Cite as: W. Jiang *et al.*, *Science* 10.1126/science.aaz7949 (2020).

Emergence of complexity in hierarchically organized chiral particles

Wenfeng Jiang[1,2,3], Zhi-bei Qu[1,2,3], Prashant Kumar[1,2], Drew Vecchio[1,2], Yuefei Wang[4,5], Yu Ma[1,2,6], Joong Hwan Bahng[7], Kalil Bernardino[8], Weverson R. Gomes[9], Felippe M. Colombari[9], Asdrubal Lozada-Blanco[10], Michael Veksler[1,2], Emanuele Marino[11], Alex Simon[1,2], Christopher Murray[11], Sérgio Ricardo Muniz[12], André F. de Moura[9]*, Nicholas A. Kotov[1,2,4,13,14]*

[1]Department of Chemical Engineering, University of Michigan, Ann Arbor, MI 48109, USA. [2]Biointerfaces Institute, University of Michigan, Ann Arbor, MI 48109, USA. [3]School of Chemistry and Chemical Engineering, Frontiers Science Center for Transformative Molecules, Shanghai Jiao Tong University, Shanghai 200240, China. [4]Department of Materials Science, University of Michigan, Ann Arbor, MI 48109, USA. [5]School of Chemical Engineering and Technology, Tianjin University, Tianjin 300072, China. [6]School of Stomatology, Lanzhou University, Lanzhou 730000, China. [7]California Institute of Technology, Pasadena, CA 91125, USA. [8]Institute of Chemistry, University of São Paulo, 05508-000 São Paulo, SP, Brazil. [9]Brazilian Nanotechnology National Laboratory (LNNano), Brazilian Center for Research in Energy and Materials (CNPEM), 13083-970 Campinas, SP, Brazil. [10]Department of Chemistry, Federal University of São Carlos, 13565-905 São Carlos, SP, Brazil. [11]Department of Chemistry, University of Pennsylvania, Philadelphia, PA 19104, USA. [12]São Carlos Institute of Physics, University of São Paulo, 13560-970 São Carlos, SP, Brazil. [13]Department of Macromolecular Science and Engineering, University of Michigan, Ann Arbor, MI 48109, USA. [14]Michigan Institute of Translational Nanotechnology (MITRAN), Ypsilanti, MI 48109, USA.

*Corresponding author. Email: moura@ufscar.br (A.F.d.M.); kotov@umich.edu (N.A.K.)

The structural complexity of composite biomaterials and biomineralized particles arises from the hierarchical ordering of inorganic building blocks over multiple scales. While empirical observations of complex nanoassemblies are abundant, physicochemical mechanisms leading to their geometrical complexity are still puzzling, especially for non-uniformly sized components. Here we report the assembly of hierarchically organized particles (HOPs) with twisted spikes and other morphologies from polydisperse Au-Cys nanoplatelets. The complexity of Au-Cys HOPs is higher than biological counterparts or other complex particles as enumerated by graph theory methods. Their intricate organization emerges from competing chirality-dependent assembly restrictions that render assembly pathways primarily dependent on nanoparticle symmetry rather than size. These findings and HOPs phase diagrams open a pathway to a large family of colloids with complex architectures and unusual chiroptical and chemical properties.

Organic-inorganic particles made by or found in living systems often display spiky, reticulated, twisted and fractal morphologies with nanoscale structural components. They can be referred to as hierarchically organized particles (HOPs) because they possess multiscale levels of organization encompassing both molecular and nanoscale structural units. Although some topological elements of their geometry can be replicated in synthetic particles with different degrees of similarity (*1*–*7*), understanding of physical mechanisms responsible for HOP formation contains many perplexing questions. One of these questions is about the origin of their complexity given the highly unfavorable thermodynamics of their template-less self-organization (*8*, *9*). The Gibbs free energy of the open structures with nanoscale organization (*10*) should be higher than that of the corresponding random, compact agglomerates (fig. S1). The latter are favored by entropy and enthalpy, and yet complex HOPs spontaneously form in multiple biological and abiological systems. Another question is about the role of polydispersity of nanoscale components involved in the self-assembly process. For similar thermodynamic reasons, the wide size distribution should favor disorganized structures, but numerous biological systems defy these expectations.

One of mechanisms guiding assembly of nanostructures could be related to the chirality of the constituent building blocks (*11*–*14*) typical for biology. However, chirality-guided self-assembly pathways are typically understood as lock-and-key mechanisms that do not permit structural variability of the components. The thermodynamic preferences of nanoparticle association based on their chirality can also be destroyed by large energy perturbations from size variations (*15*). Nevertheless, the role of chirality in assembly patterns of building blocks with wide size distribution is worth investigating further due to manifold of fundamental implications and practical implementations of chiral HOPs.

In the search for appropriate experimental systems we turned to noble-metal thiolates (*16*, *17*) as they are known to exist as one- and two-dimensional nanostructures with vari-

able surface ligands and strong chiroptical activity (*18*–*21*). We prepared chiral thiolates of gold in the form of nanoplatelets with the amino acid cysteine (Cys) as surface ligands (figs. S2 and S3 and supplementary materials) and developed their multiscale computational models (figs. S2, S4, and S5 and tables S1 and S2) that enabled us to evaluate their thermodynamic and optical characteristics. Au-Cys nanoplatelets are uniform in thickness but have a broad lateral size distribution with a dispersity index of 1.36 (fig. S2, B and C). When bearing non-racemic ligands, these particles display circular dichroism (CD) spectra with peaks in the far-UV range associated with the Cys ligands and those at the longer wavelengths associated with chirality of nanoplatelets themselves according to MD and xTB-sTDA calculations (*22*) (figs. S6 to S8 and movie S1).

The tendency of Au-Cys nanocolloids toward randomized agglomeration was mitigated by strong electrostatic repulsion imparted to particles by cetyltrimethylammonium bromide (CTAB). CTA^+ cations increasing electrokinetic zeta potential, ζ, of nanoplatelets from –18.6 mV to +44.7 mV serving as nanoscale building blocks for most particles investigated here. Association of the Au-Cys nanoplatelets, induced by high ionic strength (0.5 M NaCl) without CTAB, leads to disordered high-molecular-mass agglomerates (fig. S9). Without NaCl and CTAB, half-spiked spheroids are formed (fig. S10). These spheroids are largely disorganized but their shape is peculiar, revealing consistent symmetry-breaking with one side of the particle being smooth and the other spiky.

Adsorption of CTA^+ on the nanoplatelets increases the electrostatic repulsion, which counteracts the close-range attraction responsible for thermodynamic minima along the high-mass pathway (fig. S1). At some point, the repulsion becomes strong enough to avoid stochastic agglomeration, switching the process from the high-mass agglomeration pathway to electrostatically-frustrated self-assembly (*23*, *24*). As CTA^+ concentration is increased, the high ζ value should make edge-to-edge attachment of the nanoplatelets more favorable than the face-to-face alternative. When $[CTA^+]$ = 0.27 M, the use of pure *L*- or *D*-Cys enantiomers (enantiomeric excess χ = ±100%, see supplementary materials) produces HOPs (Fig. 1, A, B, D, and E) with twisted spikes radially organized around a common center (fig. S11); their formation is associated with the growth of strong CD bands in UV-visible and IR parts of the spectrum (Fig. 2D and fig. S12). These spiky particles will be denoted as Au-*L*-Cys and Au-*D*-Cys, respectively, or coccolith-like particles (CLIPs), cumulatively, in reference to their partial resemblance to spiky skeletons produced by microscale algae coccolithophores (*e.g.*, *Syracosphaera anthos HOL*). Despite prior studies (*8*, *10*, *25*), the unique echinate geometry of coccoliths and silicoflagellates remains a biomineralization puzzle. Statistical analysis of 500 Au-*L*-Cys CLIPs showed that they have high size uniformity with a diameter of 3.5 ± 0.3 μm and PDI = 1.02 (Fig. 1, A and B, and fig. S13).

Kayak-shaped HOPs with layered architectures, denoted as Au-*DL*-Cys, which lack the spiky geometry but do manifest hierarchical organization (Fig. 1, C and F), were observed when a racemic mixture of Cys (χ = 0%) was used. Au-*L*-Cys (Fig. 1, J and K), Au-*D*-Cys (fig. S14, A and B) and Au-*DL*-Cys (Fig. 1, L and M) possess strong light emission with red and orange colors for χ = ±100% and 0%, respectively. The confocal microscopy images (Fig. 1, J to M, and fig. S14, A and B) obtained using this intrinsic particle emission show geometries consistent with the SEM images.

The disassembly of HOPs into twisted nanoribbons by sonication reveals their hierarchical structure, composed of staggered thin sheets (Fig. 1, G and H, and fig. S14, C and D). The structural analysis of CLIPs and constituent twisted ribbons using X-ray diffraction (XRD), X-ray photoelectron spectroscopy (XPS), thermogravimetric analysis (TGA), Fourier-transform infrared spectroscopy (FTIR), UV-visible spectroscopy and time-resolved fluorescence imaging (FLIM), is consistent with atomically thin layers of gold and sulfur connected by aurophilic bonds (figs. S15 to S18). The X-ray diffraction spacing between the layers is 1.23 nm; it is nearly identical to the thickness of the Au-Cys sheets of 1.26 nm and 1.37 nm, calculated based on molecular dynamics (MD) simulations using either quantum chemical potential energy surfaces (fig. S19) or a classical force field (fig. S2A). The corresponding atomic structure of Au-Cys nanoribbons (fig. S2) forming nanosheets with [010] growth direction along the long axis can be proposed based on DFT calculations (figs. S4 and S19) and substantiated by SAXS and XRD data (figs. S3 and S15). The preference of [010] atomic structure over [100] can also be verified for twisted states of the ribbon by coarse-grained models (fig. S5 and movie S2).

The gold-thiolate nanoribbons in Au-*L*-Cys HOPs are right-handed (RH, twisted clockwise). The stacks of the corresponding nanoribbons are, however, left-handed (LH, twisted counterclockwise, Fig. 1G). The handedness of the nanoribbons and their stacks is inverted, *i.e.*, to LH and RH, respectively, if *D*-Cys is used instead (Fig. 1H). The twist of individual nanoribbons is reproduced well in atomistic MD models (Fig. 1, N to P). The staggered configuration of the ribbons assembled in a stack originates from the minimization of electrostatic repulsive forces observed previously for gold nanorods (*26*, *27*).

Strong bonding of sulfur atoms to two Au atoms and the spiky geometry associated with the molecular and submicron organization of CLIPs leads to chemical properties that are unusual for both colloidal particles and 2D nanostructures. Typical gold thiolates are known to aggregate rapidly and form precipitates (*28*), but this is not the

case for CLIPs. The spiky geometry and charged surface ligands allow this type of HOPs to form dispersions in hydrophilic and hydrophobic media with high colloidal stability (Fig. 2A and fig. S20) (*29*). They also display remarkable chemical stability, with both their geometry and bright red luminescence observed from pH 0 to 11 (Fig. 2B and figs. S21 and S22).

The dispersibility and strong luminescence of CLIPs enables elucidation of their chiroptical properties and self-assembly pathways. The spectroscopic measures for different levels of organization in CLIPs are needed as experimental order parameters to understand the dependence of self-assembly pathways to complexity on the chirality and polydispersity (fig. S1). Unlike small chiral molecules, nanoparticles, biological and (bio)inorganic nanoassemblies (*30*), this type of HOPs display strong chiroptical activity in absorption, luminescence and differential scattering simultaneously. Separation of HOPs into structural components by ultrasonication (Fig. 1, G and H, and fig. S14, C and D) as well as a diverse set of computational techniques make possible comprehensive identification of spectral signatures of all these optical processes.

The circular dichroism spectra for CLIPs show nearly perfect mirror symmetry for all the bands. Sharp peaks at 250, 310, 350, and 380 nm (Fig. 2D and fig. S23A) correspond to electronic transitions matching those calculated for model Au-*L*-Cys nanoplatelets (Fig. 2, G and H, and figs. S7 and S8). The broad 650-1350 nm band in Fig. 2D is attributed to the circularly polarized differential scattering (*31*) from the spiky particles (Fig. 2, I and J). Disassembly of these HOPs into nanoribbon stacks (Fig. 2F and fig. S23B) leads to disappearance of the peaks with maxima at 420, 560, and 830 nm, indicating that these bands are specific to the fully assembled CLIPs.

Circularly polarized light emission (CPLE) spectra of Au-*L*-Cys and Au-*D*-Cys display mirror-symmetrical strong bands at 620 nm, while their racemic counterpart, kayak-like HOPs, are CPLE-silent (Fig. 2C). There are two mechanisms how emission from HOPs acquires circular polarization. First, photons are emitted in the circularly polarized state due to angstrom-scale chirality of the excited states in the Au-Cys nanosheets (fig. S18). The chirality and, a more general case of asymmetry of the different excited states can be visualized by quantum chemical calculations (movie S1). Second, the emitted photons acquire additional circular polarization as the result of scattering on dispersed particles with submicron scale chirality. The second mechanism modifies the polarization of photons emitted by Au-Cys sheets and can revert the polarization rotation of the photons acquired during the emission. Variable contribution of scattering depending on the stage of assembly and the geometry of the HOPs, results in the variable sign of CPLE spectra. As such, the polarity of the CPLE peak of Au-*L*-Cys switches from positive (left-handed photons dominate) to negative (right-handed photons dominate) after disassembly of CLIPs into individual ribbons (Fig. 2, C and E, and fig. S24) because CLIPs have larger contribution of the differential scattering in CPLE. The same is observed for Au-*D*-Cys and constituent twisted ribbons, albeit with opposite signs of the CPLE peaks. The CD peaks in the 500-1200 nm region (Fig. 2, D and F) disappear for the constituent nanoribbons. The positive/negative CPLE peaks are, therefore, spectroscopic signatures of CLIPs, which was also confirmed by electrodynamics simulations (Fig. 2, I and J).

Combining SEM images and CPLE data, that serve as spectroscopic order parameters for this thermodynamic system, we constructed phase diagrams (Fig. 3, A to C, and fig. S25) and found a diverse spectrum of HOP phases and degrees of organization for different values of χ and building block nucleation temperature, t_n (see supplementary materials). Besides the CLIPs and kayak particles, $\chi - t_n$ diagrams include several other phases with different packing of Au-Cys sheets (Fig. 3B) and CPLE activity (Fig. 3C).

The CPLE peaks mark the evolution of the nanoscale system toward complex HOPs. However, CPLE and other chiroptical characteristics such as *g*-factor have difficulties as general enumerators of complexity because they require similarity in materials and/or geometries of the particles. For example, the *g*-factor of complex porous particle from $BaCO_3$ (*1*), $CaCO_3$ (*3*), or FeSe (*9*) with centrosymmetric geometry is ≈ 0. The *g*-factor of solid particles from gold with non-centrosymmetric geometry is ≥ 0.2 (*4*), but their complexity can be comparable to the previous particles. To address this problem, we enumerated particle complexity using graph theory (GT), extending GT approaches from chemistry (*32*) to nanomaterials (see supplementary materials). GT-based complexity index (*CI*) was calculated as augmented valence sum (*33*) with modifications ensuring its applicability across a wide range of self-assembled structures (see supplementary materials). *CI* values for a variety of particles indicate that this parameter adequately ranks them according to information content and structural sophistication (table S3). Note that other common GT indices reveal little to no correlations with particle complexity (table S4).

For the typical assemblies of nanoparticles studied before, *CI* is the range of 1.5-38.25 (fig. S26 and table S3). Analogous calculations for HOPs with the morphology of reticulated supraparticles, kayak particles, and CLIPs (Fig. 1 and fig. S11), give *CI* values of 6.0, 40.0, and 87.0, respectively (Fig. 4, A to F). Within the knowledge of nanoscale structure available for spiky coccoliths representing one of the complex biological HOPs, their *CI* is 49.0 (Fig. 4, G and H). One may note that both in the lab and in nature (molecules

responsible for biomineralization processes are homochiral), the highest structural complexity is observed for χ=100%. One may infer from that increase in complexity follows the increase in χ, which might me compelling giving the amazing complexity of biological systems. However, the relationship between χ and *CI* is non-monotonic as reflected by the *CI* calculation for different HP phases (Fig. 3D). For example, supraparticle phases 1 and 2 (SPP 1 and 2), observed for 45% < χ < 70%, have *CI* values of 2-6, which is smaller than the *CI* values of both CLIP and kayak-like particles, which may confirm the initial concerns about ability of nanoparticle chirality to guide the assembly of complex systems. The strong dependence of structural complexity on chirality can be, nevertheless, confirmed by replacement of *L*-Cys with achiral thioglycolic acid (TGA, Fig. 4, A and B). With an increasing amount of TGA, Au-thiolate particles gradually lose their organization, transitioning to random agglomerates, porous dumbbells and spheroidal particles (figs. S27 and S28) with *CI* ≤ 6 (Fig. 4). Additionally, Au-S nanoplatelets with chiral penicillamine (Pen) produce CLIPs with twisted spikes (fig. S29) similar to those from *L*- and *D*-Cys, with *CI* = 87.

The relationship between chirality and complexity in this system can be understood in the context of different restrictions on the association patterns for nanoparticles traversing the thermodynamic landscapes (fig. S1). One of the exemplary restrictions is due to electrostatic repulsion (*13*, *23*, *24*). Gradually increasing electrostatic forces in self-assembled structures lead to self-limitation of particle aggregation. Note that electrostatic restrictions result in self-limited particles exceeding 100 nm and therefore, the size variations of individual nanoparticles (2-5 nm) become insignificant (fig. S2, B and C). The resulting spheroids, however, have high size uniformity but they do not have high complexity (see SPP1, SPP2 phases in figs. S25, S27, and S28).

The complex particle architectures emerge only when restrictions on the assembly size are multiple, anisotropic, and competitive (*13*, *24*, *34*). They may be associated with different types of interactions and can be anisotropic, *i.e.* restrictions for assembly of Au-Cys nanoplatelets along their normal or in-plane axes can also vary. What is essential is that energy gains and penalties associated with these restrictions must be comparable. When none of the competing interactions and restrictions dominate, the nanoparticle assembly acquires complex architectures to negotiate these conflicting requirements. In the case of chiral nanoplatelets, anisotropic restrictions associated with electrostatic repulsion are intertwined with those from supramolecular and elastic ones. Surface energy, Frank chiral energy (*34*), and Casimir forces (*35*) contribute to the overall ΔG, but the gains and penalties associated with these interactions may not be sufficiently high to compete with restrictions from other interactions.

The comparable ΔG contribution from multiple interactions and associated restrictions on the assembly patterns force the system to acquire complex geometries. The first order assessment of energy penalties related to electrostatic, elastic, and supramolecular interactions for two chiral nanoplatelets based on MD and experimental data gives the range of 50-150 kJ/mol (*36*, *37*). For instance, the energy penalties for twisting nanoribbons (fig. S5 and movie S2) and separating two chiral NPs coated with *L*-Cys are both about 50-60 kJ/mol (*36*).

To understand better how the competitive restrictions can produce the entire spectrum of HOP phases (Fig. 3 and fig. S25) and the origin of non-monotonous dependence between chirality and complexity, an additional factor needs to be considered. While the assembly of nanoparticles can be quasi-reversible, the formation of early nanoparticles (*i.e.* the building blocks) is irreversible. Importantly, the shape of these building blocks varies for different HOPs. The early particles found at different points on the phase diagram, indeed, have diverse shapes with twisted, flat, and spheroidal geometries (Fig. 1N and figs. S30 to S33) depending on both χ and t_n. When the initial *D/L*-Au-S nanoplatelets are flat and thin, as for the kayak particles, where χ = 0% (fig. S31A), the elastic energy becomes small. The structure-defining competing restrictions for these particles are electrostatic and supramolecular related to edge-to-edge and face-to-face attachment of the nanoplatelets. Instead of the random agglomerates, the uniformly sized ribbons whose widths and stacking heights are restricted by electrostatic repulsion are formed. The kayak-like particles made from them are fairly complex, but *CI* can be increased further when elastic restrictions become more significant.

As χ increases to 30-60%, chiral asymmetry at the molecular scale increases, but particle dissymmetry and elastic restrictions disappear because the initial building blocks are large, amorphous, and spherical (fig. S32). The nearly isotropic electrostatic repulsion dominates over other restrictions, and so do the spheroidal assemblies with low *CI* represented by SPP1, SPP2, and DSP phases. The analogous conclusions can be made from the nanoassemblies made with mixed TGA/Cys surface ligands (fig. S33). When the initial particles are chiral nanoplatelets, electrostatic and elastic restrictions compete with those supramolecular ones (fig. S34). Consequently, complex HOPs with the highest *CI* emerge.

Finally, one of the key factor driving the formation of self-assembled structures with high complexity from polydispersed building blocks can be particle-particle correlations that favor specific mutual orientation of nanoparticles, such as stacking of nanoplatelets. The particle-particle cor-

relations can originate from long-range ion-correlations (*38*) and criticality of phase transitions (*39*). Phase diagram with numerous phase transitions indicates a possibility of irreversible near-critical states that can enhance interparticle correlation and dominance of particle symmetry over polydispersity (*39*).

The interplay between the different restrictions and the self-assembly pathways toward complex particles can be further visualized in HOPs obtained by doping Au-*L*-Cys with other coinage metals, such as Cu and Ag (Fig. 3, E and F, and figs. S35 to S38). The possibility for gradual 'tuning' of the competitive interactions through doping also offers the opportunity to engineer the HOP complexity. The constituent twisted nanoribbons in Au/Cu and Au/Ag HOPs displayed a pitch of 4 μm and 10 μm, respectively, indicating increased stiffness of the metal-thiolate nanosheets after doping. The elastic restrictions dominate the assembly process, which leads in the formation of simple microscale nanosheets to minimize stored mechanical energy. Consequently, a morphological transition from HOPs to long, individual nanoribbons was observed upon increasing the Ag/Au ratio (figs. S38 to S41).

Doping with Cu and Ag also enables the chiroptical properties to be tuned. The emission peaks shifted from red (620 nm) to orange (580 nm) and yellowish-green (550 nm) upon Cu and Ag doping (Cu/Au = 3.3% and Ag/Au = 16.5%, fig. S35), respectively (Fig. 3G and table S5), with concomitant changes in the CD and CPLE spectra (Fig. 3, H and I, and figs. S42 to S44) due to quantum mechanical conjugation of atomic orbitals of the coinage metals with the electronic levels of Au-Cys nanosheeds.

Thus, anisotropic electrostatic and elastic interactions place combined restrictions on the assembly pathways of chiral nanoparticles, such that the evolution of multiparticle systems becomes strongly dependent on particle symmetry and asymmetry rather than on particle size (*40*). The described phase diagrams open the door to further studies of phase transitions in systems with high dispersity, and may allow comprehensive explorations of the roles of particle chirality/asymmetry in a variety of assembly pathways. The unique optical, chemical and colloidal properties of some of the HOPs suggest their broad application in asymmetric catalysis and polarization-based opto-electronics. Assembly mechanisms involving those observed for HOPs may help us understand the origins of the astounding diversity and sophistication of biological nanocomposites.

REFERENCES AND NOTES

1. S.-H. Yu, H. Cölfen, K. Tauer, M. Antonietti, Tectonic arrangement of $BaCO_3$ nanocrystals into helices induced by a racemic block copolymer. *Nat. Mater.* **4**, 51–55 (2005). doi:10.1038/nmat1268 Medline
2. A. Gal, R. Wirth, J. Kopka, P. Fratzl, D. Faivre, A. Scheffel, Macromolecular recognition directs calcium ions to coccolith mineralization sites. *Science* **353**, 590–593 (2016). doi:10.1126/science.aaf7889 Medline
3. W. Jiang, M. S. Pacella, D. Athanasiadou, V. Nelea, H. Vali, R. M. Hazen, J. J. Gray, M. D. McKee, Chiral acidic amino acids induce chiral hierarchical structure in calcium carbonate. *Nat. Commun.* **8**, 15066 (2017). doi:10.1038/ncomms15066 Medline
4. H. E. Lee, H. Y. Ahn, J. Mun, Y. Y. Lee, M. Kim, N. H. Cho, K. Chang, W. S. Kim, J. Rho, K. T. Nam, Amino-acid- and peptide-directed synthesis of chiral plasmonic gold nanoparticles. *Nature* **556**, 360–365 (2018). doi:10.1038/s41586-018-0034-1 Medline
5. L. Zhang, T. Wang, Z. Shen, M. Liu, Chiral Nanoarchitectonics: Towards the Design, Self-Assembly, and Function of Nanoscale Chiral Twists and Helices. *Adv. Mater.* **28**, 1044–1059 (2016). doi:10.1002/adma.201502590 Medline
6. Y. Duan, X. Liu, L. Han, S. Asahina, D. Xu, Y. Cao, Y. Yao, S. Che, Optically active chiral CuO "nanoflowers". *J. Am. Chem. Soc.* **136**, 7193–7196 (2014). doi:10.1021/ja500197e Medline
7. X. Liu, F. Zhang, X. Jing, M. Pan, P. Liu, W. Li, B. Zhu, J. Li, H. Chen, L. Wang, J. Lin, Y. Liu, D. Zhao, H. Yan, C. Fan, Complex silica composite nanomaterials templated with DNA origami. *Nature* **559**, 593–598 (2018). doi:10.1038/s41586-018-0332-7 Medline
8. S. Mann, G. A. Ozin, Synthesis of inorganic materials with complex form. *Nature* **382**, 313–318 (1996). doi:10.1038/382313a0
9. D. Deng, C. Hao, S. Sen, C. Xu, P. Král, N. A. Kotov, Template-Free Hierarchical Self-Assembly of Iron Diselenide Nanoparticles into Mesoscale Hedgehogs. *J. Am. Chem. Soc.* **139**, 16630–16639 (2017). doi:10.1021/jacs.7b07838 Medline
10. J. J. De Yoreo, P. U. P. A. Gilbert, N. A. J. M. Sommerdijk, R. L. Penn, S. Whitelam, D. Joester, H. Zhang, J. D. Rimer, A. Navrotsky, J. F. Banfield, A. F. Wallace, F. M. Michel, F. C. Meldrum, H. Cölfen, P. M. Dove, Crystallization by particle attachment in synthetic, biogenic, and geologic environments. *Science* **349**, aaa6760 (2015). doi:10.1126/science.aaa6760 Medline
11. S. Pieraccini, S. Masiero, A. Ferrarini, G. Piero Spada, Chirality transfer across length-scales in nematic liquid crystals: Fundamentals and applications. *Chem. Soc. Rev.* **40**, 258–271 (2011). doi:10.1039/B924962C Medline
12. P. Duan, H. Cao, L. Zhang, M. Liu, Gelation induced supramolecular chirality: Chirality transfer, amplification and application. *Soft Matter* **10**, 5428–5448 (2014). doi:10.1039/C4SM00507D Medline
13. T. Gibaud, E. Barry, M. J. Zakhary, M. Henglin, A. Ward, Y. Yang, C. Berciu, R. Oldenbourg, M. F. Hagan, D. Nicastro, R. B. Meyer, Z. Dogic, Reconfigurable self-assembly through chiral control of interfacial tension. *Nature* **481**, 348–351 (2012). doi:10.1038/nature10769 Medline
14. T. Aida, E. W. Meijer, S. I. Stupp, Functional supramolecular polymers. *Science* **335**, 813–817 (2012). doi:10.1126/science.1205962 Medline
15. T. Shimizu, M. Kogiso, M. Masuda, Vesicle assembly in microtubes. *Nature* **383**, 487–488 (1996). doi:10.1038/383487b0
16. I. Dolamic, B. Varnholt, T. Bürgi, Chirality transfer from gold nanocluster to adsorbate evidenced by vibrational circular dichroism. *Nat. Commun.* **6**, 7117 (2015). doi:10.1038/ncomms8117 Medline
17. C. Noguez, I. L. Garzón, Optically active metal nanoparticles. *Chem. Soc. Rev.* **38**, 757–771 (2009). doi:10.1039/b800404h Medline
18. S. Cha, J. Kim, K. Kim, J. Lee, Preparation and Photoluminescent Properties of Gold (I) - Alkanethiolate Complexes Having Highly Ordered Supramolecular Structures. *Chem. Mater.* **19**, 6297–6303 (2007). doi:10.1021/cm7024944
19. B. Söptei, J. Mihály, I. C. Szigyártó, A. Wacha, C. Németh, I. Bertóti, Z. May, P. Baranyai, I. E. Sajó, A. Bóta, The supramolecular chemistry of gold and l-cysteine: Formation of photoluminescent, orange-emitting assemblies with multilayer structure. *Colloids Surf. A* **470**, 8–14 (2015). doi:10.1016/j.colsurfa.2015.01.048
20. H. Nie, M. Li, Y. Hao, X. Wang, S. X.-A. Zhang, Time-resolved monitoring of dynamic self-assembly of Au(I)-thiolate coordination polymers. *Chem. Sci.* **4**, 1852 (2013). doi:10.1039/c3sc22215b

21. C. Li, K. Deng, Z. Tang, L. Jiang, Twisted metal-amino acid nanobelts: Chirality transcription from molecules to frameworks. *J. Am. Chem. Soc.* **132**, 8202–8209 (2010). doi:10.1021/ja102827f Medline

22. S. Grimme, C. Bannwarth, Ultra-fast computation of electronic spectra for large systems by tight-binding based simplified Tamm-Dancoff approximation (sTDA-xTB). *J. Chem. Phys.* **145**, 054103 (2016). doi:10.1063/1.4959605 Medline

23. Y. Xia, T. D. Nguyen, M. Yang, B. Lee, A. Santos, P. Podsiadlo, Z. Tang, S. C. Glotzer, N. A. Kotov, Self-assembly of self-limiting monodisperse supraparticles from polydisperse nanoparticles. *Nat. Nanotechnol.* **6**, 580–587 (2011). doi:10.1038/nnano.2011.121 Medline

24. G. M. Grason, Perspective: Geometrically frustrated assemblies. *J. Chem. Phys.* **145**, 110901 (2016). doi:10.1063/1.4962629

25. J. R. Young, J. M. Didymus, P. R. Brown, B. Prins, S. Mann, Crystal assembly and phylogenetic evolution in heterococcoliths. *Nature* **356**, 516–518 (1992). doi:10.1038/356516a0

26. W. Ma, H. Kuang, L. Wang, L. Xu, W.-S. Chang, H. Zhang, M. Sun, Y. Zhu, Y. Zhao, L. Liu, C. Xu, S. Link, N. A. Kotov, Chiral plasmonics of self-assembled nanorod dimers. *Sci. Rep.* **3**, 1934 (2013). doi:10.1038/srep01934 Medline

27. M. Sun, L. Xu, J. H. Bahng, H. Kuang, S. Alben, N. A. Kotov, C. Xu, Intracellular localization of nanoparticle dimers by chirality reversal. *Nat. Commun.* **8**, 1847 (2017). doi:10.1038/s41467-017-01337-2 Medline

28. H. Nie, M. Li, Y. Hao, X. Wang, S. Gao, P. Wang, B. Ju, S. X.-A. Zhang, Morphology modulation and application of Au(I)–thiolate nanostructures. *RSC Adv.* **4**, 50521–50528 (2014). doi:10.1039/C4RA06500J

29. J. H. Bahng, B. Yeom, Y. Wang, S. O. Tung, J. D. D. Hoff, N. Kotov, Anomalous dispersions of 'hedgehog' particles. *Nature* **517**, 596–599 (2015). doi:10.1038/nature14092 Medline

30. M. Liu, L. Zhang, T. Wang, Supramolecular Chirality in Self-Assembled Systems. *Chem. Rev.* **115**, 7304–7397 (2015). doi:10.1021/cr500671p Medline

31. S. R. Kirchner, M.-N. Su, J. H. Bahng, D. G. Montjoy, W.-S. Chang, N. A. Kotov, S. Link, Scattering Properties of Individual Hedgehog Particles. *J. Phys. Chem. C* **122**, 12015–12021 (2018). doi:10.1021/acs.jpcc.8b03823

32. J.-C. Chambron, C. Dietrich-Buchecker, J.-P. Sauvage, in *Supramolecular Chemistry I—Directed Synthesis and Molecular Recognition* (Springer, 1993), pp. 131–162.

33. M. Randic, D. Plavsic, On the concept of molecular complexity. *Croat. Chem. Acta* **75**, 107–116 (2002).

34. C. Gao, S. Kewalramani, D. M. Valencia, H. Li, J. M. McCourt, M. Olvera de la Cruz, M. J. Bedzyk, Electrostatic shape control of a charged molecular membrane from ribbon to scroll. *Proc. Natl. Acad. Sci. U.S.A.* **116**, 22030–22036 (2019). doi:10.1073/pnas.1913632116 Medline

35. E. Marino, D. M. Balazs, R. W. Crisp, D. Hermida-Merino, M. A. Loi, T. E. Kodger, P. Schall, Controlling Superstructure-Property Relationships via Critical Casimir Assembly of Quantum Dots. *J. Phys. Chem. C* **123**, 13451–13457 (2019). doi:10.1021/acs.jpcc.9b02033 Medline

36. W. Feng, J.-Y. Kim, X. Wang, H. A. Calcaterra, Z. Qu, L. Meshi, N. A. Kotov, Assembly of mesoscale helices with near-unity enantiomeric excess and light-matter interactions for chiral semiconductors. *Sci. Adv.* **3**, e1601159 (2017). doi:10.1126/sciadv.1601159 Medline

37. G. I. Guerrero-García, E. González-Tovar, M. Olvera de la Cruz, Effects of the ionic size-asymmetry around a charged nanoparticle: Unequal charge neutralization and electrostatic screening. *Soft Matter* **6**, 2056 (2010). doi:10.1039/b924438g

38. N. Boon, G. I. Guerrero-García, R. van Roij, M. Olvera de la Cruz, Effective charges and virial pressure of concentrated macroion solutions. *Proc. Natl. Acad. Sci. U.S.A.* **112**, 9242–9246 (2015). doi:10.1073/pnas.1511798112 Medline

39. M. E. Fisher, The theory of equilibrium critical phenomena. *Rep. Prog. Phys.* **30**, 615–730 (1967). doi:10.1088/0034-4885/30/2/306

40. Z. B. Qu, W.-J. Feng, Y. Wang, F. Romanenko, N. A. Kotov, Diverse nanoassemblies of graphene quantum dots and their mineralogical counterparts. *Angew. Chem. Int. Ed.* (2019). doi:10.1002/anie.201908216 Medline

41. H. Chang, H. D. Jang, Controlled synthesis of porous particles via aerosol processing and their applications. *Adv. Powder Technol.* **25**, 32–42 (2014). doi:10.1016/j.apt.2013.11.004

42. H. Fan, F. Van Swol, Y. Lu, C. J. Brinker, Multiphased assembly of nanoporous silica particles. *J. Non-Cryst. Solids* **285**, 71–78 (2001). doi:10.1016/S0022-3093(01)00434-3

43. F. Caruso, R. A. Caruso, H. Möhwald, Nanoengineering of inorganic and hybrid hollow spheres by colloidal templating. *Science* **282**, 1111–1114 (1998). doi:10.1126/science.282.5391.1111 Medline

44. S. Rahmani, J. Budimir, M. Sejalon, M. Daurat, D. Aggad, E. Vivès, L. Raehm, M. Garcia, L. Lichon, M. Gary-Bobo, J.-O. Durand, C. Charnay, Large Pore Mesoporous Silica and Organosilica Nanoparticles for Pepstatin A Delivery in Breast Cancer Cells. *Molecules* **24**, 332 (2019). doi:10.3390/molecules24020332 Medline

45. M. Chirea, Electron transfer at gold nanostar assemblies: A study of shape stability and surface density influence. *Catalysts* **3**, 288–309 (2013). doi:10.3390/catal3010288

46. J. Yan, W. Feng, J.-Y. Kim, J. Lu, P. Kumar, Z. Mu, X. Wu, X. Mao, N. A. Kotov, Self-assembly of chiral nanoparticles into semiconductor helices with tunable near-infrared optical activity. *Chem. Mater.* **32**, 476–488 (2020). doi:10.1021/acs.chemmater.9b04143

47. S. Asahina, M. Suga, H. Takahashi, H. Young Jeong, C. Galeano, F. Schüth, O. Terasaki, Direct observation and analysis of yolk-shell materials using low-voltage high-resolution scanning electron microscopy: Nanometal-particles encapsulated in metal-oxide, carbon, and polymer. *APL Mater.* **2**, 113317 (2014). doi:10.1063/1.4902435

48. W. Pan, M. He, L. Zhang, Y. Hou, C. Chen, Interfacial engineering of graphene nanosheets at MgO particles for thermal conductivity enhancement of polymer composites. *Nanomaterials* **9**, 798 (2019). doi:10.3390/nano9050798 Medline

49. D. Rodríguez-Fernández, T. Altantzis, H. Heidari, S. Bals, L. M. Liz-Marzán, A protecting group approach toward synthesis of Au-silica Janus nanostars. *Chem. Commun.* **50**, 79–81 (2014). doi:10.1039/C3CC47531J Medline

ACKNOWLEDGMENTS

N.A.K. thanks Dr. David Lioi from Universal Technology Corporation, Wright Patterson Air Force Base and Prof. Sharon Glotzer of the University of Michigan for insightful discussions. A.F.M. is grateful to MEC/PET for a fellowship (2014-2020) and to CNPq for a Fellowship of Research Productivity (2020). The authors acknowledge the access to the HPC resources of the SDumont supercomputer (National Laboratory for Scientific Computing, LNCC/MCTI, Brazil, http://sdumont.lncc.br) and of the Cloud@UFSCar (http://portalcloud.ufscar.br/). W.J. thanks China Scholarship Council and Shanghai Jiao Tong University for scholarships and support. S.R.M. thanks Profs. Sebastião Pratavieira and Francisco Guimarães at IFSC/USP for technical assistance and discussions. **Funding:** This work was supported by the and Vannewar Bush DoD Fellowship to N.A.K. titled "Engineered Chiral Ceramics" ONR N000141812876, NSF project "*Energy- and Cost-Efficient Manufacturing Employing Nanoparticles*" NSF 1463474 ONR N000141812876. NSF 1566460 "Nanospiked Particles for Photocatalysis", NSF 1538180 is also gratefully acknowledged. All the authors thank the Michigan Center for Materials Characterization $(MC)^2$ for its assistance with electron microscopy, and for the NSF grant #DMR-9871177 for funding the JEOL 2010F analytical electron microscope used in this work. The authors are grateful to the Brazilian funding agencies CAPES, CNPq and FAPESP (process 2009/54035-4, 2012/15147-4, 2013/07276-1, 2013/07296-2 and 2017/12063-8) for financial support. Support for the Dual Source and Environmental X-ray Scattering Facility at the University of Pennsylvania was provided by the Laboratory for Structure and Matter which is funded in part by NSF MRSEC 1720530. E.M. and C.B.M. acknowledge support from the Office of Naval Research Multidisciplinary University Research Initiative Award ONR N00014-18-1-2497. **Author contributions:** N.A.K. conceived the project. W.J.

and N.A.K. designed the experiments. W.J. did the design, synthesis and characterization of the supraparticles, studied their chemical and chiroptical properties. S.R.M. designed, carried out and analyzed the experiments combining time and spectrally-resolved fluorescence. Z.B.Q. performed the MD simulations of the Au-Cys nanosheets. Y.W. and P.K. studied the phase diagram of Au-Cys supraparticles. Y.M. helped W.J. with some synthesis and characterizations. J.H.B. did the FDTD simulations of the CD spectra. K.B., W.R.G., F.M.C., A.L.-B. and A.F.M. carried out the DFT MD simulations, calculations of CD spectra and coarse-grained simulations of nanoparticle assemblies. N.A.K. conceived and calculated the GT models for the characterization of the complexity of different structures. E.M. measured and analyzed the small-angle X-ray scattering data. W.J. and N.A.K. co-wrote the paper. All authors contributed to data analysis, discussion and writing. **Competing interests:** Authors declare no competing interests. Nicholas A. Kotov, Jihyeon Yeom, Synthesis Of Chiral Nanoparticles Using Circularly Polarized Light, #14/940,845 - Filed: November 13, 2015, granted January 29, 2019. Nicholas Kotov, Self-Assembly Methods For Forming Mesoscale Hedgehog-Shaped Particles, Application No 62/563,966, Filed: September 27, 2017. **Data and materials availability:** All data are available in the main text or the supplementary materials.

SUPPLEMENTARY MATERIALS

science.sciencemag.org/cgi/content/full/science.aaz7949/DC1
Materials and Methods
Figs. S1 to S44
Tables S1 to S5
Movies S1 and S2
References (*41*–*49*)

9 October 2019; accepted 30 March 2020
Published online 9 April 2020
10.1126/science.aaz7949

Fig. 1 (next page). Gold thiolate hierarchically organized particles (HOPs) with cysteine surface ligands. (**A** to **C**) SEM images of Au-*L*-Cys (A), Au-*D*-Cys (B) coccolith-like particles (CLIPs) and Au-*DL*-Cys (C) kayak particles with a low magnification. (**D** to **F**) Enlarged SEM images of Au-*L*-Cys (D), Au-*D*-Cys (E) CLIPs and Au-*DL*-Cys (F) kayak particles. (**G** to **I**) SEM images and corresponding schematic illustrations of segments of Au-*L*-Cys (G), Au-*D*-Cys (H) and Au-*DL*-Cys (I). Statistical analysis of SEM images for 100 assembly segments indicates that the pitch of individual nanoribbons in the stacks is 1300 ± 123 nm and their average width is 16 ± 1.8 nm, while the average angle between two neighboring nanoribbons in the stack is 7 ± 0.7° with the pitch of nanoribbon stacks being 820 ± 10 nm. (**J** to **M**) Confocal microscopy images of Au-*L*-Cys (J and K) CLIPs, and Au-*DL*-Cys (L and M) kayak particles. (**N** to **P**) Atomistic molecular dynamics simulation of twisted conformation of Au-*L*-Cys single sheets of different lengths (N and P) and their stacks (O). Based on the XRD, XPS, and thermogravimetry data obtained for different HOPs, only Cys molecules are present in the inter-lamellar spacing between adjacent Au-*L*-Cys sheets.

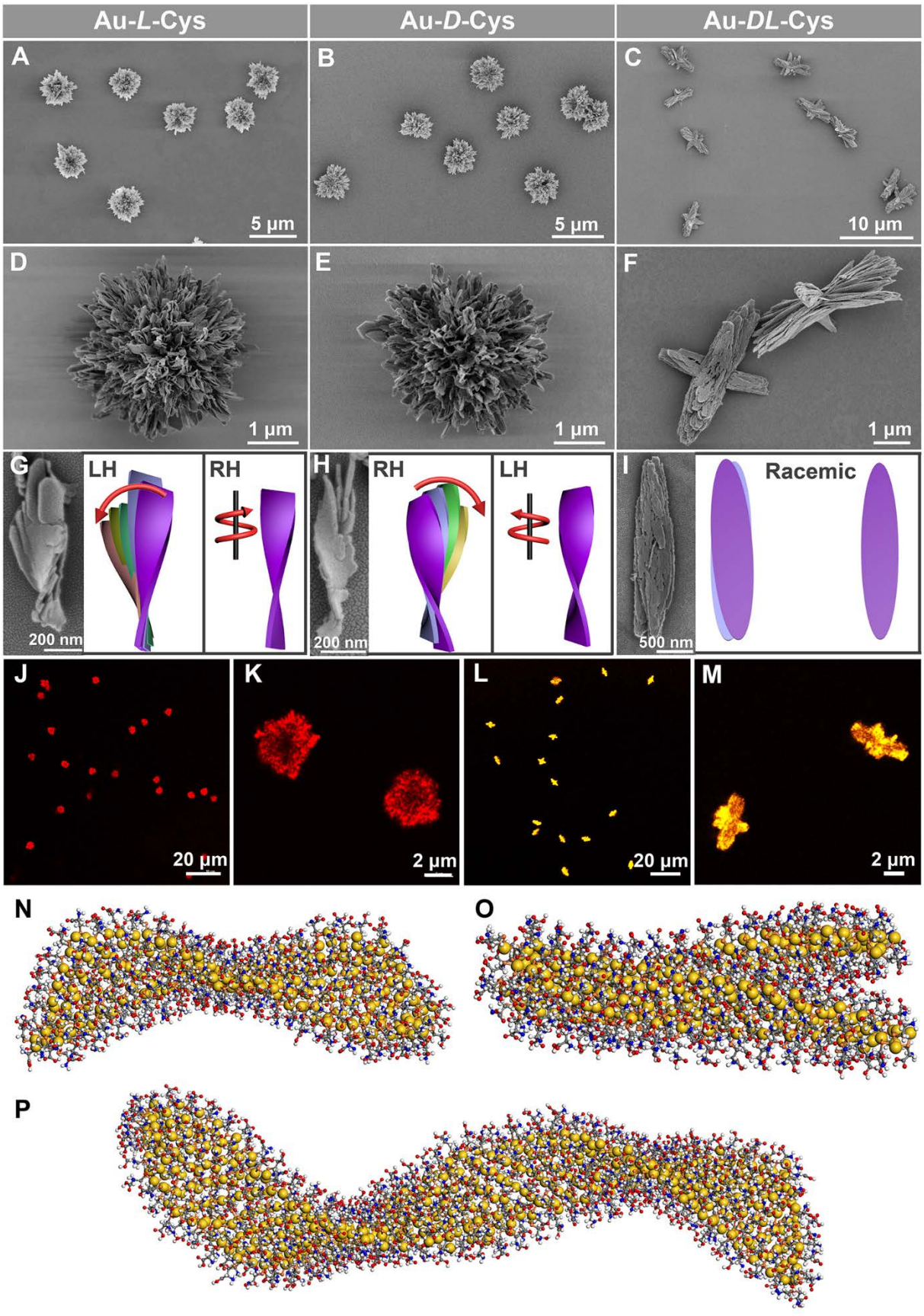

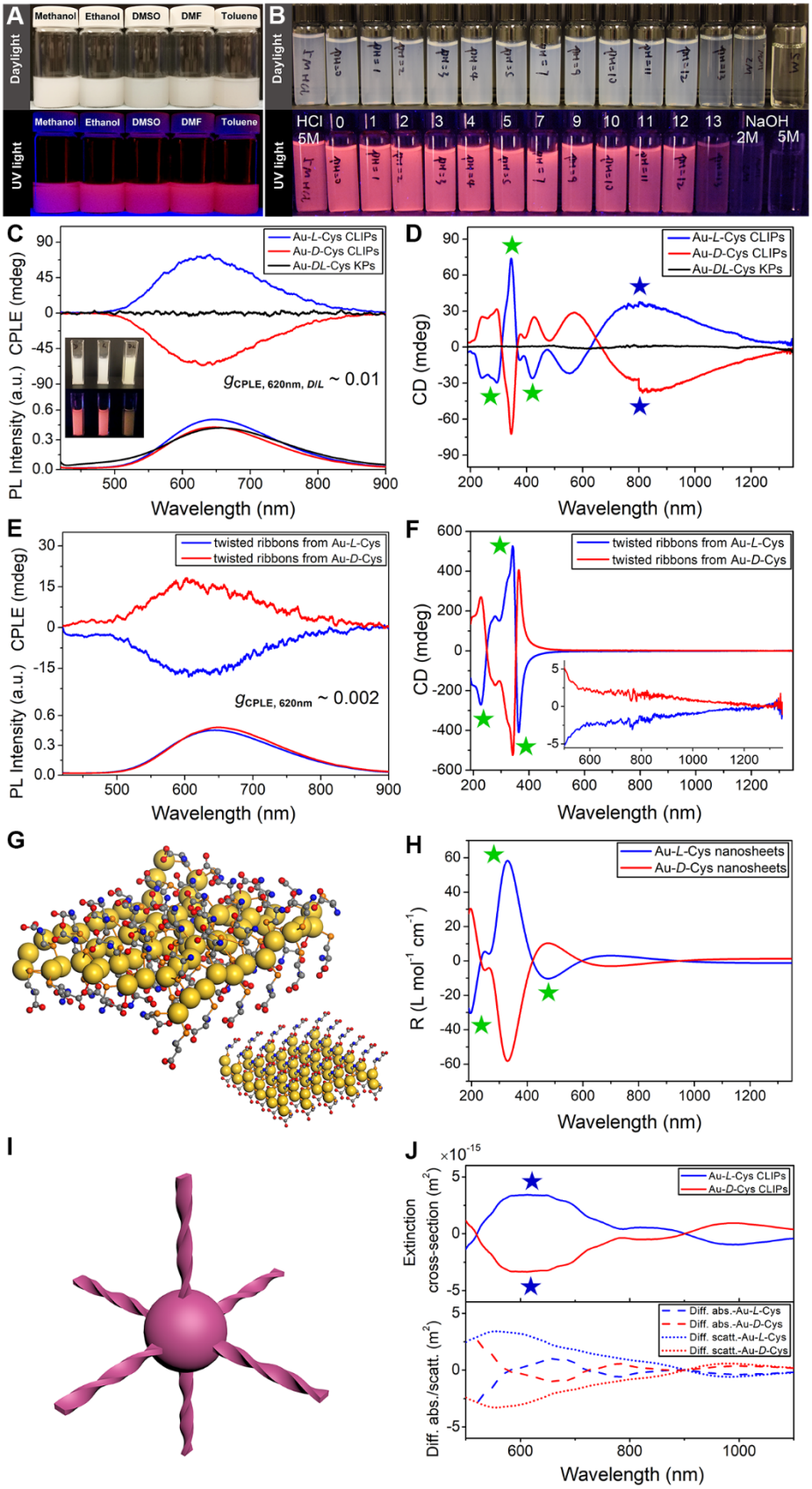

Fig. 2. Chemical and optical properties of Au-Cys CLIPs. (**A**) Dispersions of Au-*L*-Cys CLIPs in different solvents (methanol, ethanol, dimethyl sulfoxide (DMSO), *N,N*-dimethylformamide (DMF) and toluene). (**B**) Stability study of Au-*L*-Cys dispersions with different pH values or concentrations of HCl or NaOH after 12 hours. Top photograph was taken under daylight illumination and bottom photo was taken under UV light (wavelength: 365 nm) irradiation. (**C** and **D**) CPLE (C) and CD (D) spectra of Au-*L*-Cys (blue), Au-*D*-Cys (red) CLIPs and Au-*DL*-Cys (black) kayak particles. Inset in (C): photos of Au-*L*-Cys, Au-*D*-Cys and Au-*DL*-Cys dispersions under daylight and UV light illumination. (**E** and **F**) CPLE (E) and CD (F) spectra of Au-*L*-Cys (blue), Au-*D*-Cys (red) after sonication. Inset in (F): the same spectra for the 500 nm to 1350 nm spectral window to confirm the absence of the CD peaks associated with differential scattering of assembled CLIPs. The helicity of the nanoribbon stacks of Au-*L*-Cys is left-handed and, therefore, the light scattered by Au-*L*-Cys has left-handed polarization. After disassembly of the stacks into single right-handed nanoribbons, the light passing through these dispersions acquires right-handed circular polarization. (**G**) The computational model and (**H**) calculated CD spectra of Au-*L*-Cys nanoplatelets. The corresponding peaks in the short wavelength part of the CD spectra of CLIPs and nanoplatelet are marked in (D) and (F) with green stars. (**I** and **J**) The computational model and the differential extinction spectrum for the differential scattering contribution to the chiroptical properties of the CLIPs at long wavelengths. Corresponding signals in the experimental and calculated spectra in (D) and (J) are marked with blue stars.

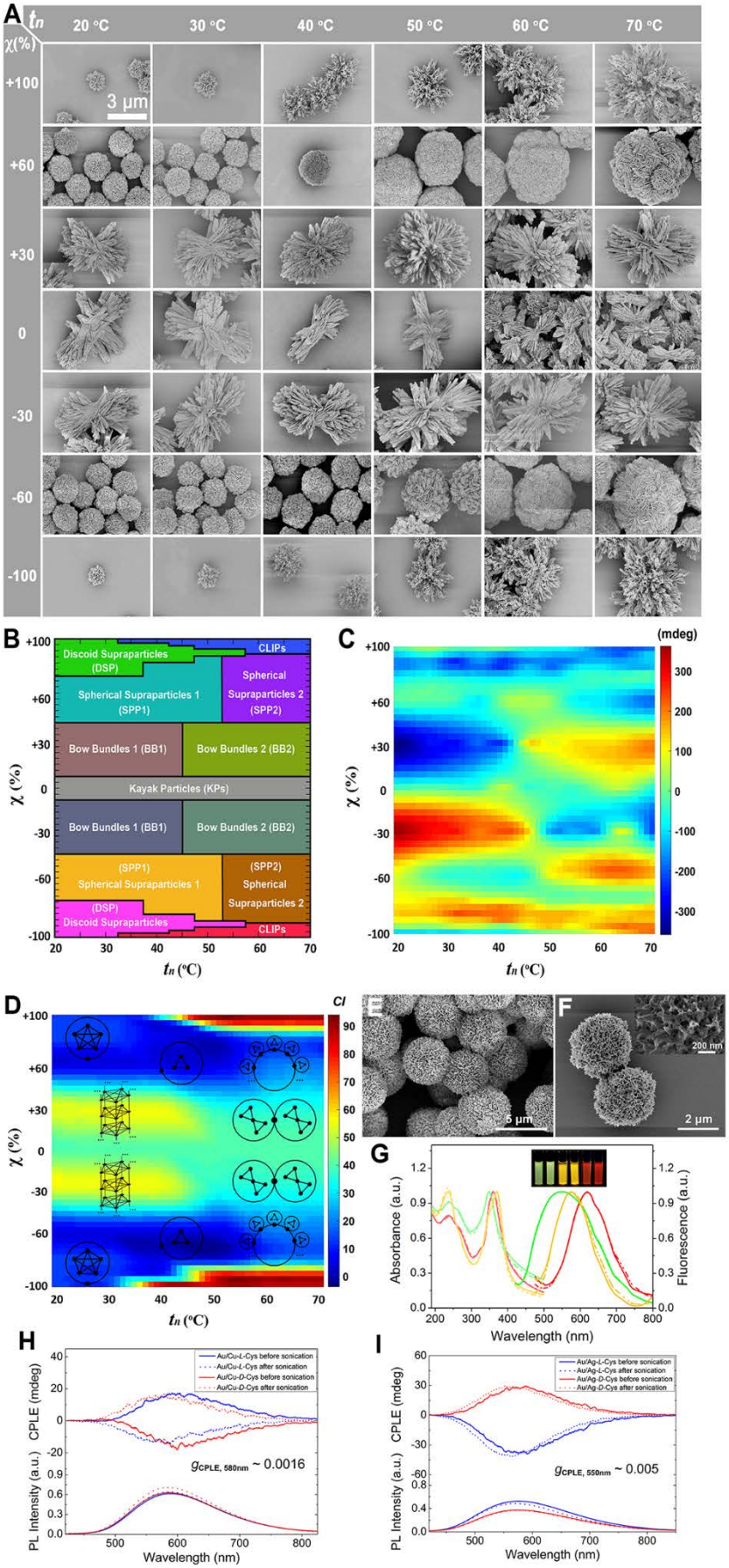

Fig. 3. Phase diagram and diversity of HOPs from chiral nanoplatelets. (**A**) SEM images of Au-Cys particles assembled at different nucleation temperatures t_n and χ values. (**B**) Phase diagram based on the geometrical description of the assembled particles. (**C**) Phase diagram based on the CPLE intensity and sign. Both types of phase diagrams display the distinct top-bottom symmetry with respect to the middle line (χ = 0). (**D**) *CI*-based phase complexity map for HOPs. GT models for phases DSP, SPP1, SPP2, BB1 and BB2 are placed for t_n and χ values where the specific phase is observed (**E** and **F**) SEM images of Au/Cu-*D*-Cys (E) and Au/Ag-*L*-Cys HOPs (F). (**G**) UV-vis and PL spectra of Au-Cys (red), Au/Cu-Cys (orange) and Au/Ag-Cys (green) samples. Solid line: HOPs obtained from *L*-cysteine; Dashed line: HOPs obtained from *D*-cysteine. Inset: photos of Au-Cys, Au/Cu-Cys and Au/Ag-Cys samples (right to left) under UV light. Numerous CD peaks were observed corresponding to molecular, nanoscale, and mesoscale levels of chirality (fig. S42). The handedness of the nanoribbons and their stacks in Au/Ag-Cys and Au/Cu-Cys was the same as those in Au-Cys CLIPs. (**H** and **I**) CPLE spectra of Au/Cu-Cys (H) and Au/Ag-Cys (I) HOPs. Solid line: before sonication; dotted lines denote spectra after sonication. The anisotropy factors for emitted photons were 0.0016 and 0.005 for Au/Cu-Cys and Au/Ag-Cys, respectively.

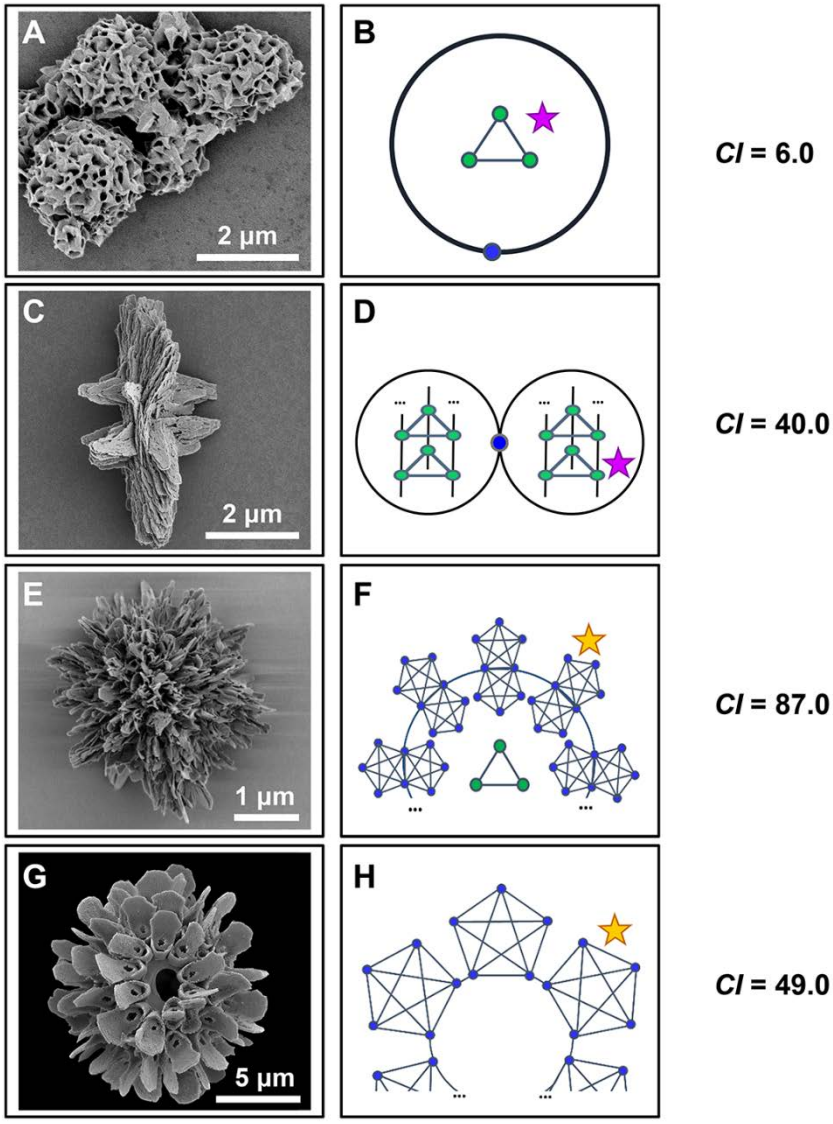

Fig. 4. SEM images of different HOPs, their GT-models, and corresponding complexity indexes (*CI*). (**A** and **B**) SEM image of supraparticle Au-thiolate with achiral TGA as surface ligands and (B) its GT-model. (**C** and **D**) SEM image of the Au-*DL*-Cys kayak-like particle and (D) its GT-model. (**E** and **F**) SEM image of the Au-*L*-Cys CLIP and (F) its GT-model. (**G** and **H**) SEM image of a skeleton of *Syracosphaera anthos HOL* reproduced from the depository of SEM images of coccoliths found at www.microtax.org and (H) its GT-model. The graph segments marked with the purple stars in (B) and (D) are MTC for the flat Au-S sheets with continuous crystallinity. The graph segments marked with the orange stars in (F) and (H) are the MTC for twisted sheets.

Emergence of complexity in hierarchically organized chiral particles

Wenfeng Jiang, Zhi-bei Qu, Prashant Kumar, Drew Vecchio, Yuefei Wang, Yu Ma, Joong Hwan Bahng, Kalil Bernardino, Weverson R. Gomes, Felippe M. Colombari, Asdrubal Lozada-Blanco, Michael Veksler, Emanuele Marino, Alex Simon, Christopher Murray, Sérgio Ricardo Muniz, André F. de Moura and Nicholas A. Kotov

published online April 9, 2020

Science (print ISSN 0036-8075; online ISSN 1095-9203) is published by the American Association for the Advancement of Science, 1200 New York Avenue NW, Washington, DC 20005. The title *Science* is a registered trademark of AAAS.